Simulation of Composite Fatigue Delamination in a Mixed-Mode Setting

Charles C. Rankin and Bryan J. Hurlbut

Rhombus Consultants Group, Inc.

NAVAIR Public Release 11-007
Distribution: Statement A—"Approved for public release; distribution is unlimited"

Abstract: For many important applications, the principal failure mode in structures built with layered composite members develops from repeated cyclic loading. Fatigue simulation adds yet another layer complexity to composite delamination response, something that has been proven very difficult to simulate with any kind of accuracy and reliability. This work introduces an approach to fatigue simulation that promises to yield results compatible with the energetics of the problem, and hence throws light onto the processes that initiate and propagate composite fatigue damage and failure.

Our approach is to build on our work based on the Goyal-Johnson formulation reported at last year's SIMULIA conference, and to add a fatigue simulation capability based on a modified Paris' law. The benefit of such a strategy is that it is based entirely on the Strain Energy Release Rates (SERR's) for each crack opening mode, permitting verification of the model with the results of coupon testing.

We shall demonstrate that our User Element (UEL) prepared from the Goyal-Johnson element can be modified for fatigue in a straightforward manner, and that several types of simulation can be performed, including direct cyclic loading and steady-state fatigue. Modifications to the Goyal-Johnson traction-separation function will be presented that eliminate several problems associated with the original formulation.

Numerical results computed with ABAQUS and our UEL will be compared with data obtained from coupon fatigue testing. Successes and problems with fatigue modeling and validation will be exposed and discussed.

*Keywords**:** Composite, Delamination, Decohesion, UEL, Traction-Separation, Traction, Non-Symmetry, Convergence, Fatigue, High-Cycle Fatigue*

1. Introduction

Advanced composite materials were developed as part of the ceaseless quest to improve structural strength and efficiency, and began to be applied to aircraft primary structures in the 1970s, seeing application in horizontal stabilizer structures of the F-14 and B-1 aircraft, and in the wing structures of the McDonnell-Douglas AV-8B. Since that time, the use of composite materials in aircraft primary structures has expanded to affect all manner of military and commercial aircraft.

Unfortunately, characterization and prediction of the fatigue behavior of advanced composite materials has proven to be a more complex problem than for metals owing to significant inhomogeneity of the material at the meso-scale (fiber-matrix interface, matrix-rich interlaminar regions, and ply drop-off, transition and splice regions). As such, tools like Paris' Law are difficult to apply or ineffective in determining the durability and safe-life of advanced composite primary structures, and structural durability has been determined by expensive life testing of key structural components.

We believe the maturity of a set of analytical techniques — referred to as progressive failure models for composite materials — allows a new approach to composite structural fatigue analysis and durability assessment to be developed that retains much of the simplicity of Paris' Law while remaining applicable to the breadth of composite constructions. In particular, we have developed a composite durability model based on a generalization of Paris' Law

$$\frac{df}{dN} = c\Delta G^{\beta} f^{k}$$

where the damage indicator (*f*) is generalized to represent damage accumulation in terms of damaged area or volume, or damage-front concentrations of stress, strain or strain-energy metrics. The Strain Energy Release Rate (SERR) ΔG is a measure of energy available to open the crack, and is often expressed as a ratio of available energy due to loading and a critical value derived from tests. Casting the load intensity in this form allows direct application of composite progressive failure techniques to the problem of fatigue damage accumulation.

It is well known that fatigue plays a role in the interlaminar de-bonding of composite materials built up from layers of differing fiber orientation. Whereas huge progress has been made in simulating the proper physics of layer separation due to normal and shear inter-laminar loading, the physics of the fatigue is less well understood, and simulation tools suffer accordingly. For this effort we selected ABAQUS as an excellent place to face the challenge of delamination fatigue. ABAQUS already has a well-established record of delamination simulation using the CO3Dxx series of elements. Since the traction-separation process is based soundly on the Strain Energy Release Rate (SERR), experience when using these elements is favorable for simple de-bonding in the presence of complex loading scenarios. In addition, ABAQUS provides a very effective user interface in the form of UEL's that permit us to experiment with the traction-separation function and examine the physics in some detail.

At the 2010 SIMULIA Customer Conference we reported our experience with CO3D8H decohesion elements for simple load-based delamination (Rankin, 2010). For that effort we constructed a UEL containing the Goyal-Johnson (GJ) formulation for traction-separation with several element topologies. Our experience has shown us that this approach leads not only to answers comparable to CO3D8H, but also had good convergence properties due to its smooth nature of the traction-separation function.

It is with our UEL that we extend our delamination capabilities to include fatigue. The next sections will cover the traction-separation function, our fatigue laws, and some simplifications based on reasonable assumptions.

2. Extended Goyal-Johnson traction separation law.

Our UEL is based on the GJ formulation (Goyal, 2003) with a few changes to add more flexibility to the shape of the traction-separation function. The traction-separation function defines the relationship between the tractions at bond interface and the measure of separation (displacement) at each element integration point, with the definitions

$$\mathbf{t} = \begin{Bmatrix} t_1 \\ t_2 \\ t_3 \end{Bmatrix}, \qquad \mathbf{s} = \begin{Bmatrix} s_1 \\ s_2 \\ s_3 \end{Bmatrix}$$

Here, the subscripts 1 and 2 refer to directions on the interfacial surface, and the subscript 3 refers to the direction normal to the interfacial surface. To facilitate mathematical definition of the constitutive model, it is convenient to introduce nondimensional expressions for the above:

$$\bar{\mathbf{t}} = \mathbf{T}_c^{-1}\mathbf{t} = \begin{Bmatrix} t_1/t_1^c \\ t_2/t_2^c \\ t_3/t_3^c \end{Bmatrix}, \bar{\mathbf{s}} = \mathbf{S}_c^{-1}\mathbf{s} = \begin{Bmatrix} s_1/s_1^c \\ s_2/s_2^c \\ s_3/s_3^c \end{Bmatrix}$$

Traction and separation quantities are related by a coupled, nonlinear function of separation and a dimensionless damage state-variable (*d*), which assumes a value greater than or equal to unity (for undamaged material $d = 1$, while for completely failed material $d \to \infty$). The functional form is exponential, and involves the "effective separation" (μ), a dimensionless scalar form of the aggregate separation field:

$$\mu = \left[\left(\sqrt{\bar{s}_1 + \bar{s}_2}\right)^{\alpha} + \bar{s}_3^{\alpha}\right]^{1/\alpha} = \left[\mu_s^{\alpha} + \mu_3^{\alpha}\right]^{1/\alpha}. \tag{1}$$

Here, α is the exponent of a power-law relation accounting for mode mixity.

The complete, non-dimensionalized, constitutive relation is expressed as a function of the effective separation and the damage state variable:

$$\begin{aligned} \bar{\mathbf{t}} &= \bar{\mathbf{s}}\, f(\mu, d : p) \\ &= \begin{Bmatrix} \bar{s}_1 \\ \bar{s}_2 \\ \langle \bar{s}_3 \rangle \end{Bmatrix} \mu^{p-1} \exp\left[p\left(2 - \mu/d - d\right)\right] - \begin{Bmatrix} 0 \\ 0 \\ \langle -\bar{s}_3 \rangle \end{Bmatrix} \kappa \end{aligned} \tag{2}$$

Note that *p* is a parameter that adjusts the shape of the traction-separation curve. The brackets $\langle \bullet \rangle$ denote the Heaviside step function, which takes the value of its argument when the argument is positive, and a value of zero when the argument is non-positive. One will note that the behavior of the Heaviside function determines that the last term of Equation 2 applies only when the surface-normal separation is *negative*, implying crack closure. Thus, the model described by Equation 2 directly incorporates stiffness against free-surface interpenetration.

The damage state (d) evolves under monotonic loading according to the rule

$$d_{n+1} = \max\left(1, d_n, \mu_{n+1}\right). \tag{3}$$

Note that Equation 3 preserves irreversibility of the damage state.

Figure 1 shows a plot of the traction-separation functions for shear- and normal-separations and no damage ($d = 1$).

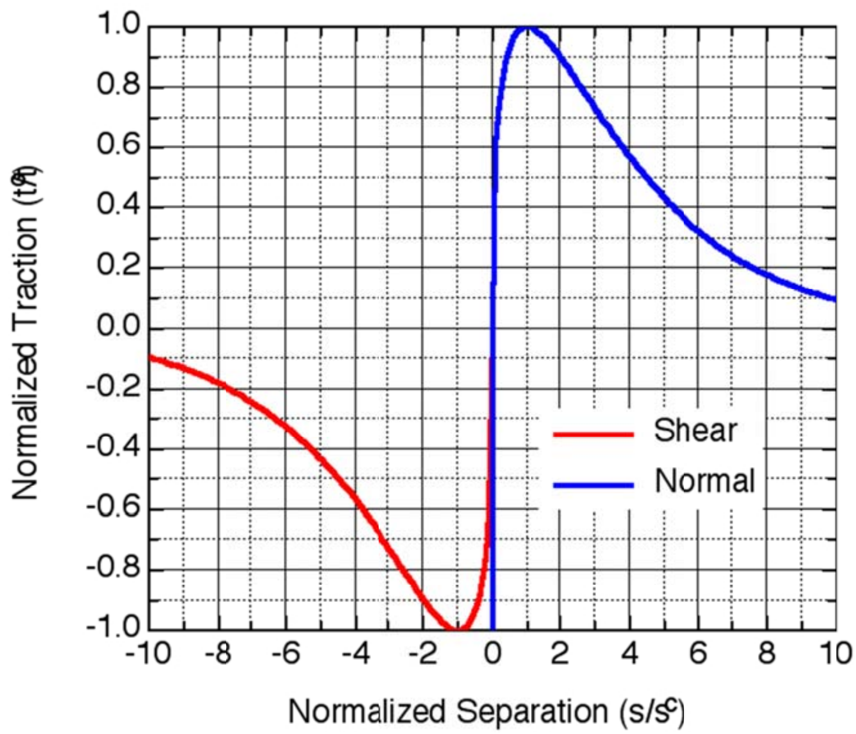

Figure 1. Normalized modified GJ traction-separation function

A simple analysis shows that the integral for the energy release

$$G_C = \int_0^\infty \mathbf{t} \cdot d\mathbf{s} \tag{4}$$

leads to the formula

$$\left[\frac{G_I}{G_{IC}}\right]^{\alpha/2}+\left[\frac{G_{II}}{G_{IIC}}\right]^{\alpha/2}=1$$

which is a power-law based failure relationship. Our modification to the GJ function is found in the new term μ^{p-1} that causes the function to rise steeply for initial separations; we have found this essential when handling shear, since actual shear displacements can be quite small before the onset of damage. The factor *p* in the exponent preserves the normalization. We have also implicitly assumed that the norm of the dimensionless shear term is indifferent to any direction lying on the delamination surface, with direction 3 (normal) treated separately.

With our form of the GJ traction-separation law, we have been able to prevent spurious displacements along the debonding surface without requiring overly high critical shear tractions t_1^c and t_2^c.

3. Fatigue laws

The decohesive constitutive model simulates the direct fracture process through the irreversible damage-accumulation law, Equation 3. Accumulation of fatigue damage is modeled on a cyclic basis according to a power-law relation

$$\partial d/\partial N = d,_N = \lambda\left(G/G_C\right)^k. \tag{5}$$

Determination of the loading intensity $\left(G/G_C\right)$ requires determination of the instantaneous available SERR (*G*). The integral in Equation 4 evaluates to

$$G_i = \left(t_i^c s_i^c\right)\left(e/p\right)^p \Gamma(p+1, p\mu_i) \tag{6}$$

where $\Gamma(p+1, p\mu)$ is the incomplete gamma function. The load intensity function can then be expressed as

$$\frac{G_i}{G_C}=\frac{\Gamma(p+1, p\mu_i)}{\Gamma(p)}=P\left[2(1+p), p\mu_i\right] \tag{7}$$

where $P[\bullet]$ is the statistical Chi-squared distribution with 2(1+p) freedoms (about 2.6 for useful ranges of parameters).

For single-mode fatigue, the power-law parameters (λ, k) can be determined to fit measured crack-growth rates in canonical specimens. For general, mixed-mode loading, we have employed the following combination of single-mode parameters:

$$
\begin{aligned}
d_{,N} &= \frac{1}{\mu}\Big[\left(\mu_s\lambda_s\right)^{\alpha} + \left(\mu_3\lambda_3\right)^{\alpha}\Big]^{1/\alpha}\Big[\Delta\left(G/G_C\right)\Big]^{\bar{k}} \\
\bar{k} &= \frac{1}{\mu}\Big[\left(\mu_s k_s\right)^{\alpha} + \left(\mu_3 k_3\right)^{\alpha}\Big]^{1/\alpha}
\end{aligned}
\tag{8}
$$

4. Fatigue correlation with coupon tests

To validate our model, we used results from (Zhu, 2008) to provide the parameters in Equations 5 and 8 that best fit the test data. Three types of specimens are in that report: a Double Cantilevered Beam (DCB) test series for determining the normal critical shear, an End Notched Flexture (ENF) test series for determining pure shear response, and Single Leg Beam (SLB) test series for determining a mode mixture of about 42 percent shear. Critical SERRS for these three cases are G_{1c} =1.39 (normal), G_{2c} =8.02 (shear), and G_{Tc} =1.85N/mm (SLB combined loading). The latter mixed-mode test series fixes the exponent α to about 1.27, based on the energetics of the combined load case. Fatigue testing yielded the results plotted in Figure 2 based on the SERR values listed above.

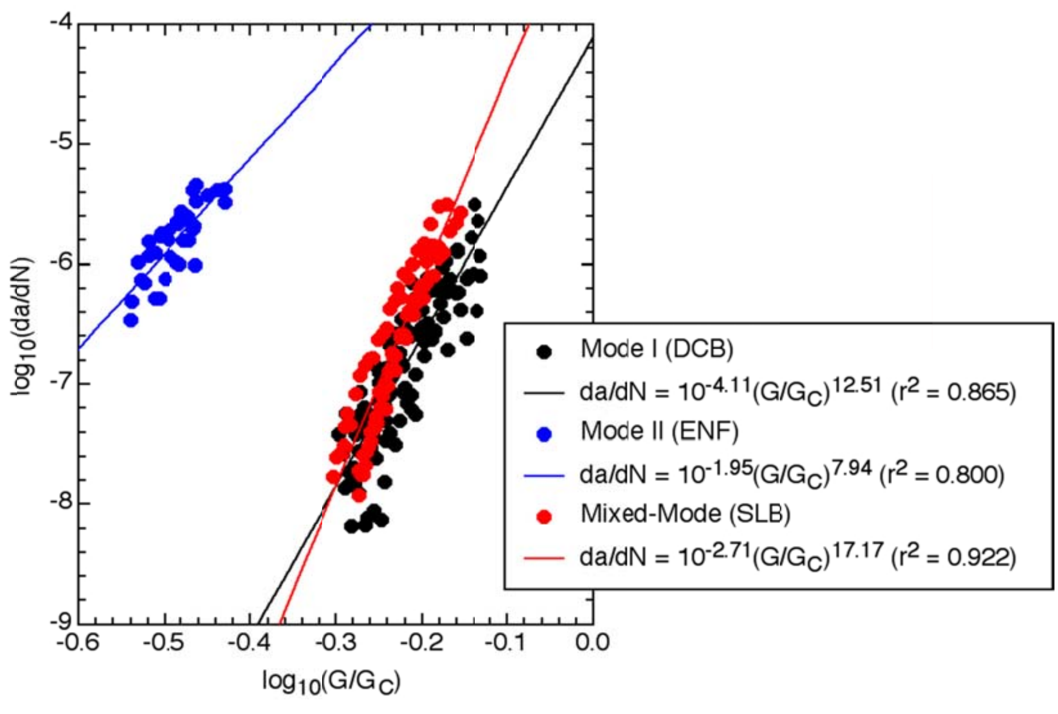

Figure 2. Paris Law Fits for the Three Fatigue Test Series

Before we started with the fatigue simulations, we noticed immediately how sensitive the measured Paris exponents are to the degree of mixity. We must first note that the exponents for all three series of tests are quite high, which implies some degree of sensitivity to the exponent choice, and therefore likely very difficult to obtain reliably from a limited test series. Even more interestingly, the mixed mode exponent based on this test series does not lie between the Mode I and Mode II, but instead is much higher. It is not surprising that correlation with current simulation models presents a serious challenge.

5. ABAQUS UEL options

Three types of records are required in the ABAQUS job input file to activate our GJ UEL implementation. These are:

1) *ELEMENT records defining the user-element nodal connectivities;
2) *USER ELEMENT record(s) defining the user element type (U1), number of nodes and coordinates per node, numbers of integer- (4) and floating-point (14) properties, number of element state variables, and active degrees of freedom per node (3 or 6);
3) *UEL PROPERTY record(s) defining the floating-point and integer properties for each user-element set.

Floating-point valued user-element properties are specified first, followed by integer-valued properties. The properties, in order of specification are:

Floating-Point Values:

G_{IC}	Mode I SERR
G_{IIC}	Mode II SERR (primary surface direction)
G_{IIC}	Mode II SERR (secondary surface direction)
t_3^c	Critical traction (normal direction)
t_1^c	Critical traction (primary surface direction)
t_2^c	Critical traction (secondary surface direction)
κ	Penalty stiffness
α	Mode-mixity exponent
λ_3	Fatigue scaling parameter (normal direction)
k_3	Fatigue-law exponent (normal direction)
h	Shell offset parameter (zero value implies ½ shell thickness)
λ_s	Fatigue scaling parameter (surface directions)

k_s	Fatigue-law exponent (surface directions)
ε	Normalized separation at which ½ of t_3^c is achieved (sets *p*)

Integer Values:

INTGS	Integration: Gaussian (1), Newton-Cotes (2), Simpson's Rule (3)
NIPX	Number of integration points in primary surface direction
NIPY	Number of integration points in secondary surface direction
KFIELD	(presently not used)

The number of element-state variables should be set to 15*NIPX*NIPY+1 at minimum, since fifteen quantities are saved in the element-state vector for each element integration point. The last entry in the element-state vector is the number of cycles of fatigue accumulated at that element integration point.

The option of choice for fatigue is the so-called "steady state" case, where multiple cycles identical loading are executed with the assumption that basic load path through the delaminating interface changes little for a given group of cycles. If the load path in the surrounding area changes little, Equation 8 can be integrated for that particular group of loading cycles, yielding the number of cycles as a function of the decohesion state. Any number of steady-state runs can be made with updated system configurations.

6. Fatigue simulation results & conclusions

Using Equation 8 as the fatigue law, we obtain the following selected data fits, shown in Figures 3–5, below. Figure 3 shows measured and predicted crack-growth behavior for DCB sample 4–2 in (Zhu, 2008), Figure 4 shows crack growth for ENF sample 5–3 in (Zhu, 2008), and Figure 5 shows crack-growth for SLB sample 6–1 in (Zhu, 2008). Note, in all of these Figures, wide variations in the multiplier and exponent produce relatively indistinguishable fits to the measured data.

For example, Figure 3 indicates fairly similar data fits of the Mode I fatigue law

$$d_{,N} = \lambda_3 \left(G_I / G_{IC} \right)^{k_3} \tag{9}$$

to DCB sample 4–3 (Zhu, 2008) for (λ_3, k_3) equal to (30,10) and (150,12). This wide variation of exponents indicates that the large fatigue-law exponents only weakly affect damage accrual, since cyclic damage accrual occurs at SERR fractions of the order of 50 percent ($0.5^{12} = 2.44 \cdot 10^{-4}, 0.5^{10} = 9.77 \cdot 10^{-4}$). The principal characteristic determined by the fatigue-law exponent is the effective curvature of the $a(N)$ curve. Since the dataset is too sparse and variable to admit reliable computation of d^2a/dN^2, we fear that greater precision in choosing the fatigue-law exponent will not be forthcoming in a straightforward manner.

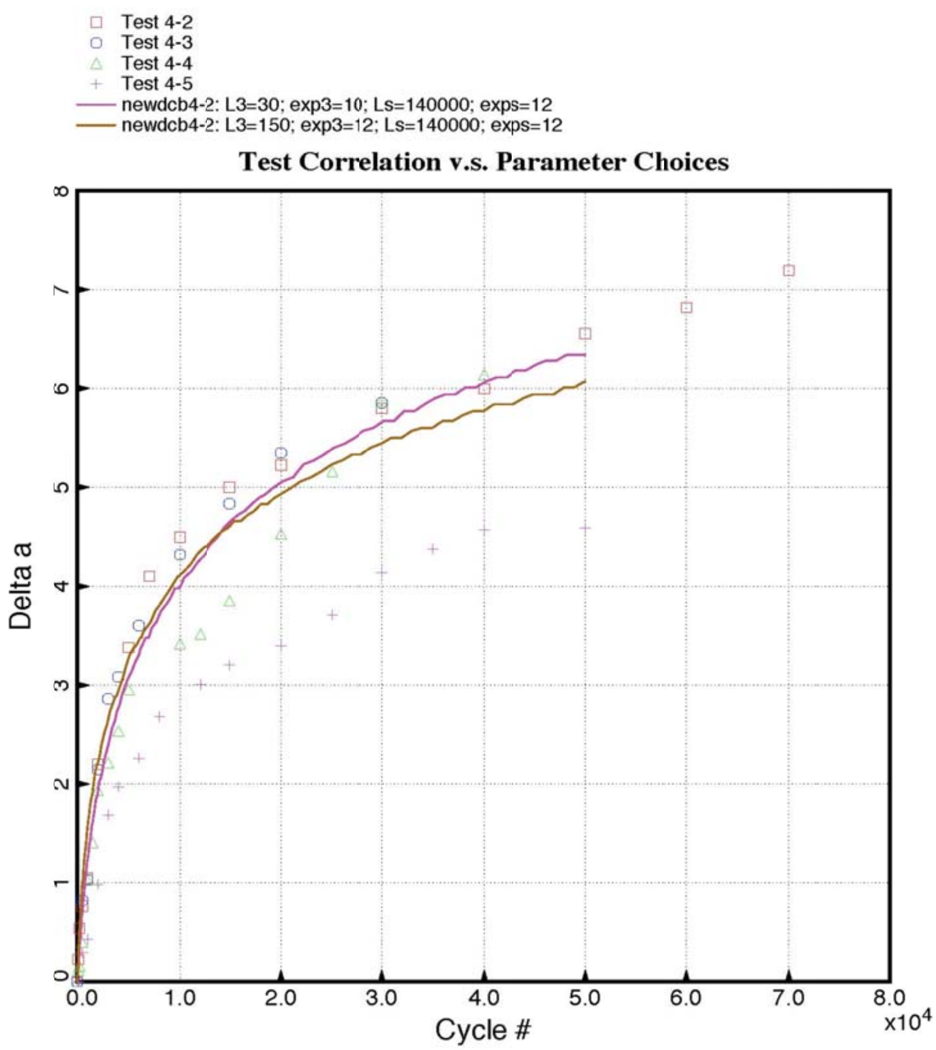

Figure 3. Measured and Predicted Crack-Growth for DCB Test Samples

Similar characteristics are evident in parameter choices illustrated in Figure 4. Here, (λ_S, k_S) parameters in the range (3200,9) to (150000, 12) all fit ENF sample 5–3 **(**Zhu, 2008) relatively closely, especially admitting that reducing the constant slightly has the desired effect of reducing damage accrual rate.

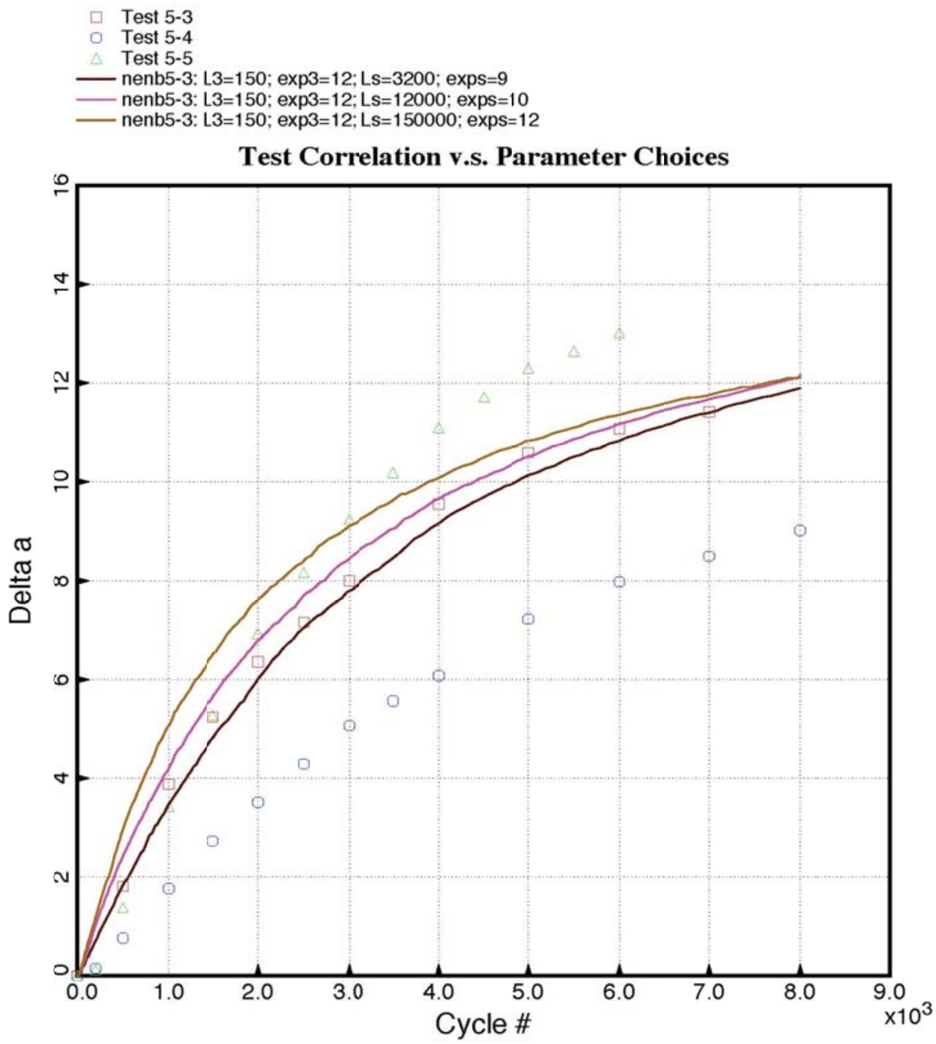

Figure 4. Measured and Predicted Crack-Growth for ENF Test Samples

Figure 5 is perhaps most instructive, as it shows that damage accrual rate can be modulated at will using either Mode I or Mode II parameters. In this case, all exponents have been kept at the same value, while crack-growth response has been increased in simulation simply by independently increasing the fatigue-law constant multipliers. One will immediately see from the figure that correlation was difficult for this limited set of test data. Clearly, we would like to be able to extract suitable parameter sets from single-mode tests for use in mixed-mode simulations. This is simply not possible at this stage of the game. The fatigue law parameters, as we have constituted them in Equations 8 and 9, cannot be uniquely determined, nor do they combine in the manners indicated to accurately predict mixed-mode responses. Instead, some alternative postulate is needed at this juncture.

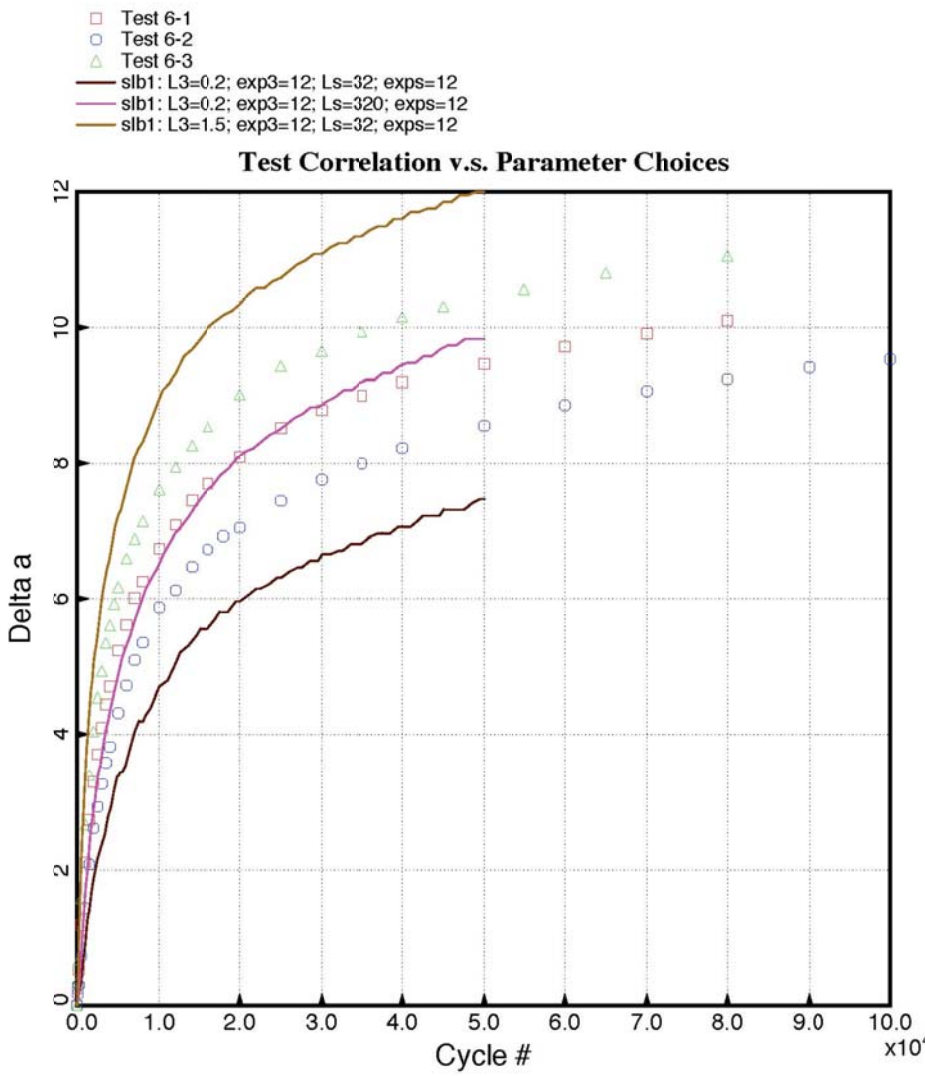

Figure 5. Measured and Predicted Crack-Growth for SLB Test Samples

We can gain some insight by examining the history of energy dissipation at selected points along the fracture path. Figure 6 shows normalized traction-separation histories for representative points along the fracture paths of DCB, ENF and SLB simulation models. All of these cases have $s_S^c = s_3^c$. Also shown, in red, is the undamaged traction-separation relationship of Equation 2 with $p = 0.35$. The numbers in parentheses indicate the SERR fraction corresponding to each curve's integral. Naturally, the undamaged (i.e. static) constitutive model integrates to 100 percent of the assigned SERR.

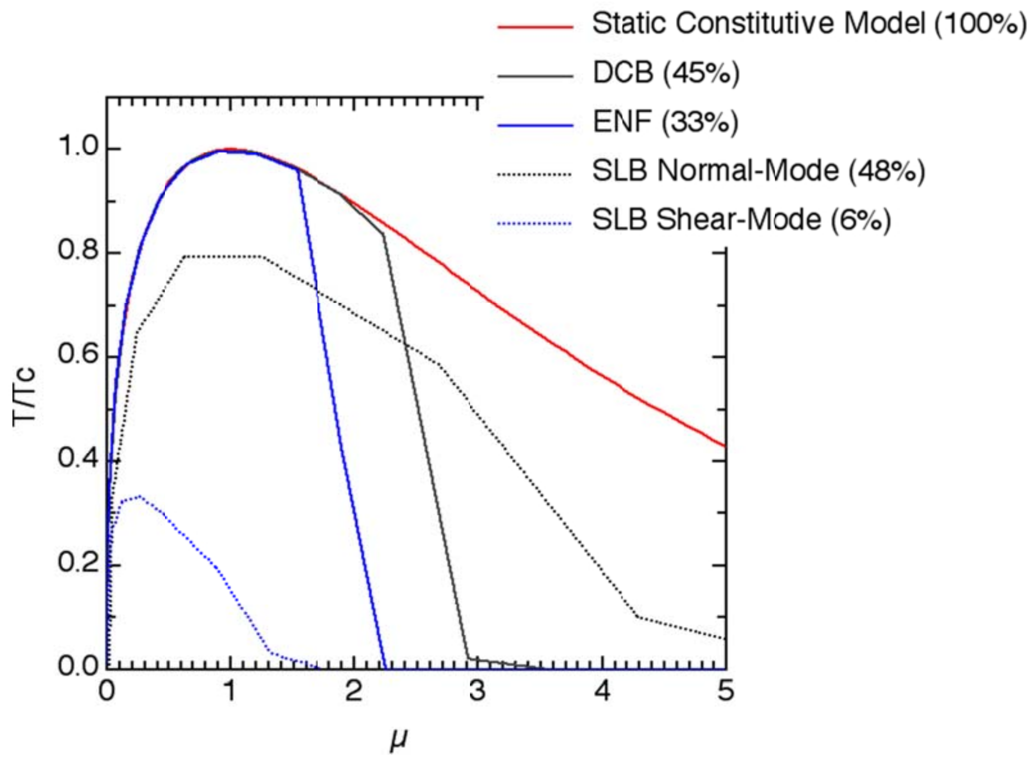

Figure 6. Normalized Traction-Separation Histories for selected DCB, ENF and SLB Locations

It is of interest to note the differing energy fractions associated with failure in each specimen type. The point chosen in the DCB-sample model undergoes some 5620 cycles to dissipate 45 percent of the material's G_{IC}, whereas the point chosen in the ENF-sample model undergoes only 199 cycles to dissipate 33 percent of G_{IIC}. In each case, use of the SERR fraction to represent the load intensity results in accrual of significant damage only after critical separation is reached (i.e. $\mu > 1$, note that $G/G_C = 16.6\%$ at $\mu = 1$). Fatigue damage in the DCB sample accrues significantly after $\mu > 2$, while fatigue damage in the ENF sample becomes significant at $\mu > 1.5$.

It is not so straightforward to determine onset of fatigue damage for the SLB case from Figure 6. This is because no convenient analog of normalized interfacial traction is available in the mixed-mode case. One aspect that is quite evident, however, from Figure 6 is that fatigue damage spreads over a larger range of interfacial separation in the mixed-mode case than in either single-mode case.

Another noteworthy aspect of Figure 6 is that the fraction of Mode II energy relative to total fracture-dissipated energy for the SLB mixed-mode fatigue failure is 0.40, as would be expected from the test-sample geometry.

To understand better the kinetics of failure progression in the mixed-mode case, Figure 7 shows accrued damage and mode-specific normalized separations versus generalized separation. Note that no damage is accrued while the generalized separation falls below unity. Damage is accrued along the “quasi-static” portion of the generalized traction-separation curve when $d = \mu$ (dashed line). One may think of such damage as accruing due to redistribution of strain energy ahead of the advancing crack. Eventually, sufficient SERR is available to produce significant damage according to the fatigue law. At this point, the damage curve departs the quasi-static damage line (dashed) and increases markedly due to fatigue damage.

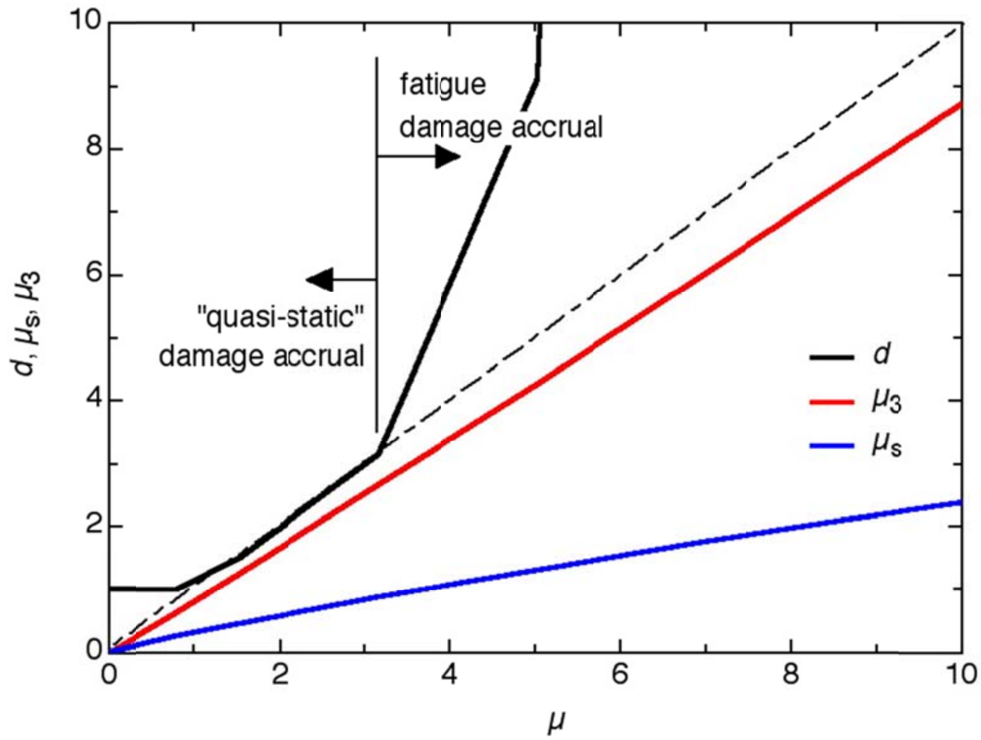

Figure 7. Damage Parameter and Mode-Specific Separations vs. Generalized Separation for SLB, Mixed-Mode Failure Progression

Note also in Figure 7 that normal separation (μ_3) is much, much higher than shear separation (μ_S). This indicates that Mode I failure is by far the greatest contributor to crack propagation in the SLB coupon. This fact is also evident by virtue of the measured SLB G_C (0.171 N/mm for the SLB vs. 0.146 N/mm for the DCB and 0.802 N/mm for the ENF).

Recourse to Figure 7 confirms that the progression of failure in the SLB model occurs in a manner similar to the DCB and ENF, in that damage is initiated quasi-statically, with fatigue-generated damage becoming significant only subsequently. The total energy dissipated by fracture at the selected SLB-model point is 69 percent of the critical energy, or effectively 0.118 N/mm. In contrast, total energy dissipated in fatigue failure of DCB and ENF sample-models are 0.066 N/mm and 0.265 N/mm, respectively.

The fact that our parameter-correlation test cases does not admit selection of a single set of parameters for single- and mixed-mode cases indicates that our formulated fatigue law in Equation 8 cannot be expected to hold in the general case. Thus, validation of the present model with respect to test data is not possible. Instead, alternative forms of the fatigue law may be required.

All simulations were run on a Dell Precision workstation running RedHat Linux. The workstation has 2 Intel XEON Irwindale processors running at 3.0 GHz, and 3.0 Gb of RAM. The complete fatigue simulations were run on models varying from 6,024 to 15,624 equations, and had CPU run times averaging 600 seconds.

7. Summary

With this work, we have demonstrated that fatigue simulation can be correlated with coupon tests for both Mode I and Mode II fracture. All the physics is based on the SERR, and the energy dissipation at the fracture front has been examined in some detail. The outstanding problem is to predict mixed-mode fracture based on the Mode I and Mode II results in a consistent manner. This, we believe, is the main challenge for systems with such huge Paris exponents. It is entirely possible that extensions or generalizations to our current fatigue formulations will be required.

8. References

1. Rankin, C.C, Regelbrugge, M.E., and Hurlbut, B.J., "Advanced Decohesion Elements for the Simulation of Composite Delamination," 2010 SIMULIA Customer Conference, Providence RI, 2010.
2. Goyal, V.K. and Johnson, E.R., "Cohesive-Decohesive Interfacial Constitutive Law for the Analyses of Fatigue Crack Initiation and Growth," AIAA CP 2003-1678, Proc. 44th AIAA/ASME/ASCE/AHS Structures, Structural Dynamics, and Materials Conference, Norfolk, Virginia, 7-10 April 2003.
3. Zhu, Y, "Characterization of Interlaminar Fracture Toughness of a Laminated Composite Material," Masters Thesis, The Pennsylvania State University, Dept. of Engineering Science and Mechanics, 2008.

9. Acknowledgements

We wish to acknowledge the support of NAVAIR under Contract N68333-06-0355